Static analysis and optimization design of a small grass-grid laying device

Jing Sheng[1*], Yongwei Chen[1,2], Guoman Liu[1], Shunhu Deng[1], Hao Xu[1]

(1. *College of Mechanical Engineering, Jiangxi University of Water Resources and Electric Power, Nanchang 330099, China*; 2. *College of Transportation, Nanchang Jiaotong Institute, Nanchang 330100, China*)

Abstract: With the growing global focus on environmental protection, desertification control has attracted widespread attention. Traditional manual straw checkerboard sand barrier laying is limited by low efficiency and high labor costs. This study presents the development of a compact straw checkerboard laying device to replace manual operation and achieve efficient, low-cost desertification control. Mathematical analysis, Matlab-based parameter optimization, and finite element analysis (FEA) were performed to support the lightweight design of the device frame and core straw-pressing roller. A scaled demonstration prototype was fabricated, and comparative tests were conducted to verify the optimization effect. The optimized straw-pressing roller achieved a 17.87% weight reduction with nearly unchanged mechanical properties, with performance fully meeting the material strength requirements. Comparative tests confirmed no significant difference in working performance between the pre- and post-optimized rollers. This device satisfies the standard requirements of straw checkerboard laying, providing a technical reference for the development of lightweight sand fixation equipment.

Keywords: small grass-grid laying device, grass-pressing wheel, desert control, optimal analysis, static analysis

DOI: 10.25165/j.ijabe.20261904.9737

Citation: Sheng J, Chen Y W, Liu G M, Deng S H, Xu H. Static analysis and optimization design of a small grass-grid laying device. Int J Agric & Biol Eng, 2026; 19(4): 133–142.

1 Introduction

China is one of the countries most severely affected by desertification worldwide, with sandy land accounting for approximately 27% of its total territorial area[1]. Desertified land is distributed across most provincial-level administrative regions in China, and is mainly concentrated in eight provinces and autonomous regions: Qinghai, Xinjiang, Inner Mongolia, Tibet, Gansu, Shaanxi, Ningxia, and Hebei[2]. According to official statistics, the annual economic loss caused by desertification in China exceeded 64 billion CNY as of 2020. At present, the laying of straw checkerboard sand barriers is widely recognized as one of the most effective technical measures for windbreak and sand fixation.

In recent years, to address the severe challenge of desertification, the field of windbreak and sand fixation has developed rapidly, and domestic and international scholars have conducted extensive research and development (R&D) on straw checkerboard sand barrier laying machinery. Qi et al.[3] developed an integrated rice straw checkerboard laying and pressing machine. The structural design was informed by measured rice straw properties including bundle length, repose angle, and elastic modulus, while the distribution and pressing system was validated through 3D modeling and multibody dynamic simulation. Optimal operating parameters were derived via response surface methodology optimization. Field tests in desert environments confirmed that core indicators including straw output, layer thickness, and burial depth all met quality standards, demonstrating the machine's applicability for desertification control engineering. Wang et al.[4] designed a hand-held miniaturized straw checkerboard sand barrier paver, and completed the design and mechanical analysis of its core component, the straw-pressing wheel. They concluded that the optimal diameter of the straw-pressing wheel for this equipment was 850 mm. Chang[5] developed a small straw checkerboard sand fixation machine based on the working environment of straw checkerboard laying equipment and specific design requirements. Considering comprehensive working conditions, the straw-pressing disc of the machine was designed as a disc structure with a radius of 600 mm and a thickness of 6 mm. Peng et al.[6] designed a portable straw checkerboard sand barrier laying vehicle to address the low automation level of manual straw checkerboard barrier installation. They completed the design of core mechanisms including straw insertion and conveying via 3D modeling, and verified the strength of key components through load tests and finite element simulation. Prototype tests confirmed stable operation of the equipment, providing a reference for the research and development of sand control equipment.

He et al.[7] innovatively designed the mechanical structure for a small-scale straw checkerboard sand barrier robot, including a ditching device integrated with a cam and double crank combined adjustment mechanism. This design resolved the drawbacks of complex structure and excessive space occupation of conventional ditching devices. The robot can relieve workers from heavy manual labor, and boasts the merits of high laying efficiency, superior trafficability, and excellent laying quality. Li et al.[8] developed a multi-functional three-dimensional desert sand-fixation and grass-planting machine fitted with an automatic straw laying system. During traveling, the machine can peel off straw preloaded in the straw hopper at a preset thickness, which slides down onto the sand trough. The straw-pressing and soil covering assembly then presses the straw into the sandy soil to complete the full straw laying operation. Ye et al.[9] designed a compact straw checkerboard laying

Received date: 2025-02-17 **Accepted date:** 2026-06-25

Biographies: Yongwei Chen, MS, research interest: motor control, Email: 2061442866@qq.com; **Guoman Liu**, PhD, research interest: control science and engineering, Email: liuguoman@126.com; **Shunhu Deng**, MS, research interest: mechanical engineering, Email: 1420886032@qq.com; **Hao Xu**, MS, research interest: mechanical engineering, Email: 3040845747@qq.com.

***Corresponding author: Jing Sheng**, PhD, Associate Professor, research interest: design of intelligent mechanical equipment, digital signal processing. No. 289 Tianxiang Avenue, High-Tech Development Zone, Nanchang 330099, China, Tel: +86-15279190885, Email: jing.sheng@juwp.edu.cn.

machine. Compared with traditional straw laying equipment, this machine adopts worm gear and worm drive to control the straw-pressing depth of the laying wheel, while realizing the retraction and deployment of the straw laying mechanism. The machine can freely adjust the straw laying volume according to the field environment, and regulate the required straw feed rate by controlling its forward speed.

Lin et al.[10] proposed an intelligent integrated straw checkerboard laying device. The 50° serrated straw-pressing blade of the device reduces the insertion resistance into desert sand, improves operation accuracy, and enables the device to perform straw checkerboard sand barrier laying operations in a variety of working conditions.

2 Main structure design

The compact straw checkerboard laying device consists of four functional modules: chassis module, seeding module, straw checkerboard laying module, and straw-pressing module. The straw curtain storage and conveying mechanism is driven by a motor via a gear drive, which rotates the storage reel to deliver the wheat straw curtain to the straw-pressing wheel equipped with limit stop branch chains, followed by cutting via the cutting assembly. The cutting assembly comprises a cutter, linkage mechanism, fixed arm, push rod, lead screw, and drive motor. The limit stop branch chains of the straw curtain conveying mechanism engage with the straw-pressing wheel to tension the straw curtain, ensuring stable cutting. The cutter, initially in the closed state, is moved to the center of the straw curtain by the lead screw, and the push rod and linkage mechanism then actuate the cutter to open rapidly for cutting. Subsequently, the lead screw drives the upper push rod, fixed arm, and cutter to move backward for secondary cutting, achieving complete severing of the straw curtain.

During the laying operation, the straw curtain is pressed into the sandy soil by the straw-pressing wheel. In this process, the drive motor powers the gear mechanism, which drives the lead screw to move the matched sliders. This structure converts rotational motion into linear motion, enabling the vertical lowering and sand penetration of the straw-pressing wheel. The straw-pressing wheel adopts a crank-linkage force amplification structure to increase the compaction force applied to the straw curtain.

The sand compaction assembly consists of a crank-rocker mechanism, sand compaction rod, and drive motor. During the straw checkerboard laying process, the motor at the rear end of the assembly is activated, and the crank-rocker mechanism drives the sand compaction rod to perform reciprocating linear motion at a 45° downward angle. This motion compacts the sandy soil, which enhances the sand fixation effect and improves the structural stability of the laid straw checkerboard. A schematic diagram of the compact straw checkerboard laying device is shown in Figure 1.

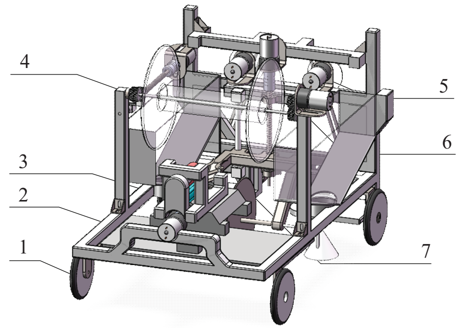

1. Driving wheel 2. Chassis 3. Grass curtain cutting device 4. Grass curtain conveying device 5. Covering soil device 6. Grass-pressing wheel lifting device 7. Grass-pressing wheel

Figure 1 Schematic diagram of the device structure

2.1 Rack design

The chassis module is the core component of the compact straw checkerboard laying device, responsible for bearing the overall weight of the equipment and providing stable mounting support for all other functional modules. It is mainly composed of an elevated base, frame, and dual-drive transmission system. The front end of the frame provides mounting support for the cutting assembly of the device; the middle section supports the straw curtain storage reel assembly; and the rear end provides mounting support for the lifting mechanism of the straw-pressing wheel and the sand compaction assembly. The structural schematic of the frame is shown in Figure 2.

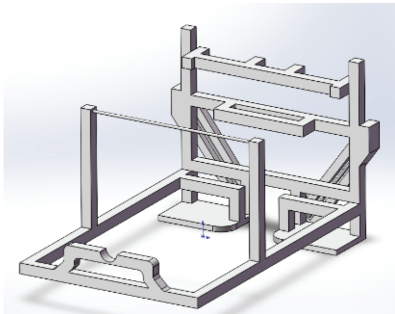

Figure 2 Rack structure diagram

2.2 Grass-pressing wheel design

The working environment for straw checkerboard laying is typically desert areas, with more complex operating conditions than those of general construction machinery. Therefore, the core performance requirements for the straw-pressing roller are as follows: low rolling friction and slip rate while ensuring sufficient driving force; adequate penetration capacity to meet the straw laying depth requirements; and excellent operational stability of the whole machine during travel[11,12].

The straw-pressing roller assembly rotates under the action of contact friction between the roller and the sandy ground during operation. When the straw-pressing roller rotates at a constant speed in desert sandy soil, the dead weight of the roller and the whole device makes the roller press into the sandy layer, leaving ruts on the sandy ground as it rotates. The supporting reaction force exerted by the sandy soil on the contact point of the straw-pressing roller consists of a normal force denoted as R and a tangential frictional force denoted as T[13]. The internal friction torque of the wheel axle, the friction torque between the wheel axle and the bearing, and the load torque from the drive transmission mechanism are collectively denoted as Mg. The force conditions of the straw-pressing roller are shown in Figure 3. These parameters are the key factors affecting the contact characteristics between the straw-pressing roller and the desert sandy ground.

When the grass roller is in a balanced state, there is:

$$P = Rx \tag{1}$$

$$G = Ry \tag{2}$$

$$P_{\mathrm{rd}} = Gd + M_m + M_k + M_g \tag{3}$$

where, P is axial supporting force, N; G is longitudinal supporting force, N; P_{rd} is resultant rotational force, N.

According to the force analysis, when the grass roller is in a purely rolling state, it represents the optimal state for pressing the grass. That is,

$$R_x > P \tag{4}$$

$$P_{\mathrm{rd}} > Gd + M_m + M_k + M_g \tag{5}$$

In the actual working process of the grass-pressing wheel, the required traction force is determined by the walking resistance. The traction force is directly proportional to the walking resistance[14]. Typically, the resistance of the grass-pressing wheel consists of the compaction resistance of sandy soil, the resistance due to pushing, and others. However, when the grass-pressing wheel works to a certain depth, the compaction resistance increases and becomes the main influencing factor on the grass-pressing wheel[15]. At this point, the friction resistance of the device can be neglected. The simplified resistance of the grass-pressing wheel is shown in Fig 4.

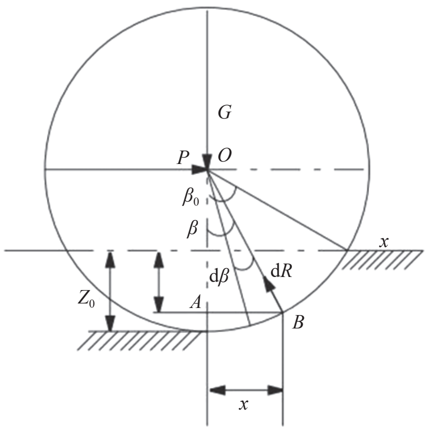

Figure 3 Schematic diagram of the force on the grass compression wheel

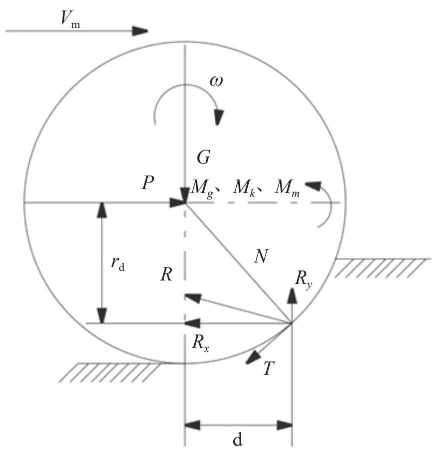

Figure 4 Schematic of grass-pressing wheel support reaction force and external resistance

Based on the force diagram of the grass-pressing wheel, it can be concluded that:

$$G = \int \mathrm{d}R\cos\theta \tag{6}$$

$$\mathrm{d}R = -bpr\mathrm{d}\theta \tag{7}$$

$$\cos\theta = \frac{\mathrm{d}x}{r\mathrm{d}\theta} \tag{8}$$

$$G = -b\int_x^0 p\mathrm{d}x \tag{9}$$

Due to the fact that

$$p = kz^n \tag{10}$$

$$2x\mathrm{d}x = -D\mathrm{d}z \tag{11}$$

$$\mathrm{d}x = -\frac{D\mathrm{d}z}{2x} = -\frac{\sqrt{D}\mathrm{d}z}{2\sqrt{Z_0 - Z}} \tag{12}$$

$$G = kb\int_0^{Z_0} z^n \frac{\sqrt{D}D}{2\sqrt{Z_0 - Z}}\mathrm{d}z \tag{13}$$

Assume that $t^2 = Z_0 - Z, -\mathrm{d}z = 2t\mathrm{d}t$
and,

$$G = kb\sqrt{D}\int_0^{Z_0}(Z_0 - t^2)^n\mathrm{d}t \tag{14}$$

Expanding $(Z_0 - t^2)^n$ Taylor gives

$$G = kb\sqrt{D}\left(\frac{3-n}{3}Z_0^{n+\frac{1}{2}}\right) \tag{15}$$

$$Z_0 = \left[\frac{2G}{(3-n)kb\sqrt{D}}\right]^{\frac{2}{2n+1}} \tag{16}$$

where, Z_0 is depth of subsidence, mm; G is vertical load, i.e. the device's own gravity, N; k is soil property index; n is depth index; b is width of grass-pressing wheel, mm; D is grass-pressing wheel diameter, mm.

From Equation (16), the subsidence depth of the grass-pressing wheel is closely related to the soil characteristics, its own gravity, and the specifications of the grass-pressing wheel itself[16,17]. Using Matlab to calculate Equation (16), the surface cloud diagram of the device self-weight G, the grass-pressing wheel diameter D, and the thickness b were obtained at the sinking depth of 200 mm, as shown in Figure 5. When G is 41.35 kg, D is 600 mm, and b is 10 mm, the device can meet the sinking depth work requirement of 200 mm. The diagram of the model is shown in Figure 6.

According to the calculation results, the model of disc-shaped grass-pressing wheel with D of 600 mm and b of 10 mm was established in 3D modeling software. At this size, the self-weight of the grass-pressing wheel is 22.069 kg.

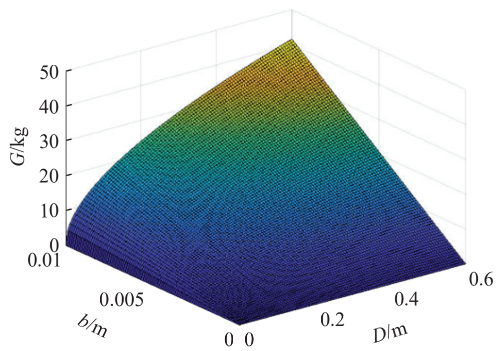

Figure 5 Cloud diagram of G, D, b relationship

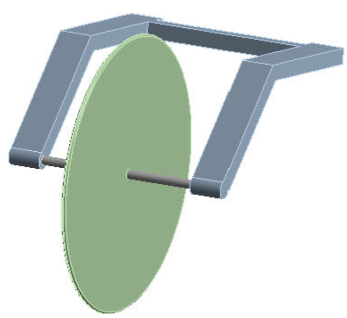

Figure 6 Model diagram of the grass-pressing wheel module

3 Finite element analysis of key parts

3.1 Theory of static analysis

Statics is mainly used to analyze the response of a structure under static loading, such as deformation, stress, and strain of the structure. The basic equation for static analysis is

$$[K]\{\delta\} = \{F\} \tag{17}$$

where, $[K]$ is overall stiffness matrix of the model; $\{\delta\}$ is model overall displacement matrix; $\{F\}$ is overall model load matrix.

The fourth strength theory is used to determine whether a structure has failed. The fourth strength theory equation is

$$\sigma_{eq} = \sqrt{\frac{1}{2}\left[(\sigma_1-\sigma_2)^2(\sigma_2-\sigma_3)^2(\sigma_3-\sigma_1)^2\right]} < [\sigma] \tag{18}$$

where, σ_{eq} is Von Mises stress; $\sigma_1,\sigma_2,\sigma_3$ are first principal stress, second principal stress, and third principal stress[16]; $[\sigma]$ is material permissible stress.

Inertia and damping can be neglected when the structure is subjected to static loads[17]. Static loads are those that are constant and unchanging, where the structure is in static equilibrium or where the change with time is very slow, and some constant inertia loads can also be treated as static load[18].

3.2 Establishment of a finite element analysis model

Accurate geometric representation is the core prerequisite for establishing a valid finite element analysis (FEA) model of the frame, which forms the fundamental basis of the entire FEA work. In this study, the three-dimensional (3D) model of the frame established in SolidWorks is exported and converted into the x_t format, which is compatible with ANSYS Workbench software. The model is subsequently simplified by ignoring geometric features with negligible impact on the analysis results, including minor holes, slots, and other fine structures in non-critical areas[19]. This simplification process strictly balances modeling accuracy and computational efficiency, as improper model simplification will lead to a significant deviation between the FEA results and the actual mechanical properties of the frame.

Considering the complex and harsh desert operating conditions of the compact straw checkerboard laying device and the large bearing load of the frame, Q235 structural steel is selected as the fabrication material for the frame. The key physical properties of the material are listed in Table 1.

Table 1 Material properties of Q235 structural steel

Parameter	Value
Modulus of elasticity/GPa	200
Density/kg·m^{-3}	7850
Poisson's ratio	0.3
yield strength/MPa	235

3.3 Grid division

Following the establishment of the validated finite element analysis (FEA) model of the device frame, mesh discretization is implemented in strict compliance with four core criteria for static FEA: geometric feature fidelity, stress field gradient matching, balance between computational accuracy and efficiency, and numerical convergence guarantee. The 10-node second-order tetrahedral solid element is adopted for full-model discretization, which can accurately fit the frame's complex geometric boundaries and ensure high-precision calculation in stress concentration regions. Based on the frame's overall dimension, minimum characteristic size of the main structural section and pre-simulation convergence results, the global mesh size is set to 3.0 mm, which ensures the geometric integrity of the main structure while effectively controlling computational cost. Targeted mesh refinement is performed in high stress gradient regions prone to stress concentration, including structural fillets, openings, section mutations, and load/constraint boundaries. The size ratio of adjacent meshes is strictly controlled within 1.5 to ensure smooth size transition and avoid numerical oscillation. All key mesh quality indicators are controlled within the allowable threshold for static FEA. Mesh independence verification confirms that the relative change of key mechanical response indices is less than 5% under this scheme, meeting the preset accuracy requirements. The final mesh model contains 568 496 nodes and 289 206 elements, with the meshing result shown in Figure 7.

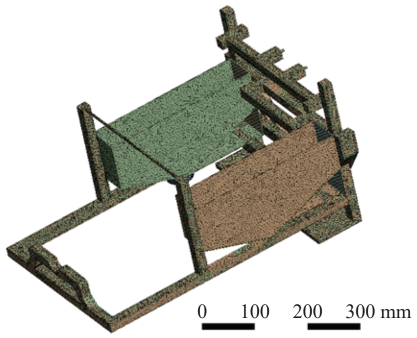

Figure 7 Grid division diagram

3.4 Adding boundary conditions

Based on the actual operational characteristics of the compact straw checkerboard laying device, only the core loads are considered in the application of boundary conditions for the frame finite element analysis (FEA): the dead weight of the whole device, the pressure load exerted by the straw curtain, and the gravity load from other functional modules mounted on the frame. The specific boundary conditions applied to the device frame are shown in Figure 8. A concentrated gravity load of 400 N from the other functional modules of the device is applied to the frame; meanwhile, a 5 MPa pressure load corresponding to the working reaction force is applied to the frame, together with the dead weight of the whole device.

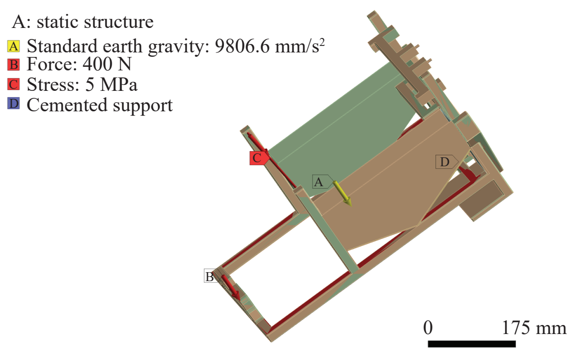

Figure 8 Schematic diagram of boundary conditions

3.5 Model solution and result analysis

After the solution calculation is completed in ANSYS Workbench, the contour plot of the total deformation of the device frame under load is obtained, as shown in Figure 9. It can be seen from the figure that the maximum deformation of the frame occurs at the front end of the frame, i.e., the mounting position of the cutting assembly, with a maximum deformation value of 0.356 19 mm. This region is the convergence point of multiple forces on the frame, with highly concentrated applied loads, which results in a relatively large deformation at this position.

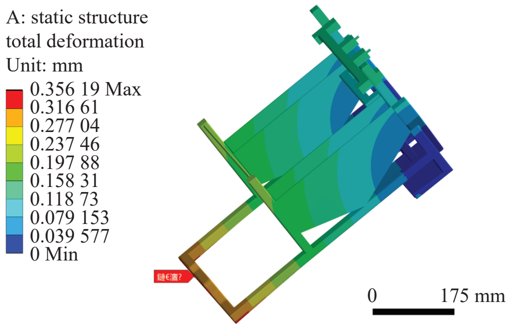

Figure 9 Cloud diagram of total deformation of grass compressor with the installation of the frame

The equivalent stress contour plot of the device frame obtained from the solution calculation is shown in Figure 10. It can be seen from Figure 9 that the maximum stress of the device frame under load is 108.97 MPa, which occurs at the recessed position of the frame, while the stress levels in the rest of the regions are relatively low. The frame is fabricated from Q235 structural steel, which has a standard yield strength of 235 MPa. To avoid fatigue failure of the frame under normal operating conditions, a safety factor is introduced, and the allowable stress of the material is calculated via Equation (19).

$$[\sigma] = \frac{\sigma_s}{n} \tag{19}$$

where, σ_s is yield strength of Q235 structural steel, MPa; n is safety factor, taken as 1.25.

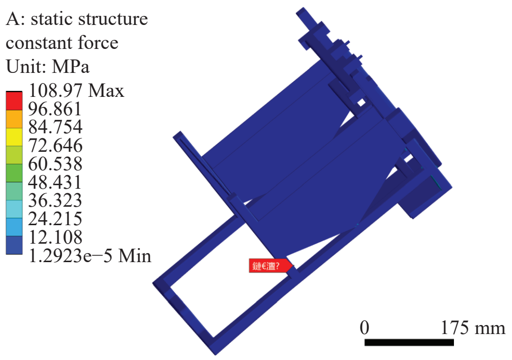

Figure 10 Equivalent force cloud

It can be concluded that the maximum stress of the installation of the frame after loading is 108.97 MPa, which is less than the yield strength of 188 MPa after taking the safety factor of the material, so the strength and stiffness of the structure meet the design requirements.

3.6 Finite element analysis of grass roller

Due to the relatively complex and harsh desert environment in which the device works, as well as the large load supported by the grass pressure wheel, the material of the grass pressure wheel should be Q235 structural steel. Its material physical properties are listed in Table 1.

The grid cell size of the grass-pressing wheel is set to 2 mm, generating 131 310 grid nodes and 72 512 meshes, and the grid is refined in the parts that are prone to stress concentration, so that the grid transition is uniform. The effect of the mesh division of the grass-pressing wheel is shown in Figure 11.

Due to the working characteristics of the device, which moves at a low speed, the device only takes into account the self-weight of the device as well as the compaction resistance and traveling resistance during the working of the grass roller. The boundary conditions are imposed as shown in Figure 12. A pressure of 1000 N is applied to the edge of the grass roller in contact with the sand; in addition, a rotational speed of 3 rad/s is added to the grass roller.

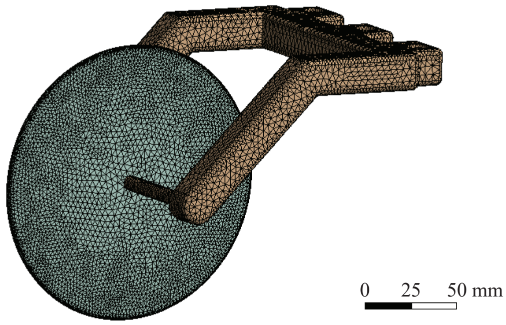

Figure 11 Grid division

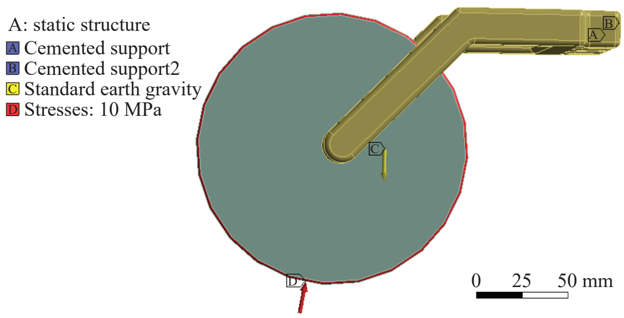

Figure 12 Boundary conditions

After the ANSYS Workbench software solution calculation to obtain the total deformation of the grass-pressing wheel loaded cloud diagram shown in Figure 13, it can be found that the maximum deformation of 1.1501 mm occurs at the edge of the grass-pressing wheel directly in contact with the ground, due to the grass-pressing wheel is the multi-force convergence point with the load applied more centralized.

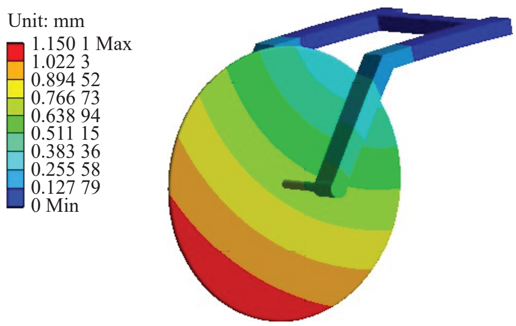

Figure 13 Cloud diagram of total deformation of grass roller

The equivalent stress cloud diagram of the grass roller obtained after calculation is shown in Figure 14. It can be concluded that the maximum stress of the grass roller after loading is 75.98 MPa, which occurs in the depression of the front end of the roller, and the stresses in the rest of the parts are relatively low. The material of the grass roller is Q235 structural steel, and its maximum yield limit strength is 235 MPa. In order to ensure that no fatigue failure occurs in the normal operation of the grass roller, a safety coefficient is set, and the permissible stress is obtained as in Equation (19).

From this, it can be concluded that the maximum stress of the grass roller after loading is 75.98 MPa, which is smaller than the yield strength of the grass roller material after taking the safety coefficient of 188 MPa, so the strength and stiffness of the grass roller structure meet the design requirements.

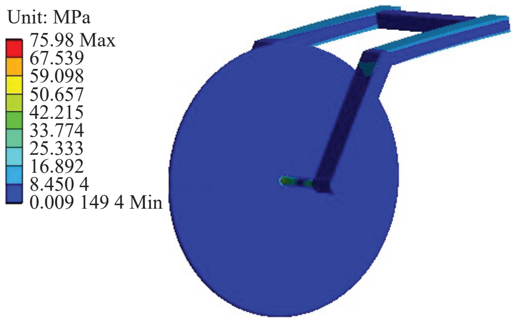

Figure 14 Equivalent force cloud of grass roller

4 Topology optimization of grass roller

The overall dimensions of the grass-pressing roller device have been verified to fully meet the operational requirements of grass square lattice laying. On this basis, structural topology optimization is carried out for the roller body, with the core engineering objectives of reducing structural mass, cutting material consumption, and lowering the rotational inertia to improve the operational efficiency of the device. The optimization is implemented under the premise of fully satisfying the mechanical performance requirements (i.e., structural stiffness and load-bearing capacity) of the roller during grass square laying operations, so as to achieve a balanced design between working performance and light weight.

In this study, the Solid Isotropic Material with Penalization (SIMP) optimization method is adopted to establish the numerical optimization model. The core principle of the SIMP method is to map the relative density of each finite element to its elastic modulus through a penalty interpolation function, driving intermediate density elements to converge to 0 (void, material removed) or 1 (solid, material retained), to finally obtain the optimal material distribution in the design domain.

4.1 SIMP-based topology optimization model

For the grass-pressing roller, the inner hub area matches with the rotating shaft, the outer rim contact surface matches with the grass square, and the axial positioning end faces are set as the non-design domain (the relative density of elements is fixed at 1, unchangeable during optimization), to ensure the assembly accuracy and operational reliability of the roller. The web area between the hub and the rim is set as the design domain, which is the core optimization object for material distribution adjustment.

The design domain is discretized into finite elements, and the relative density of each element in the design domain is taken as the design variable[20], defined as:

$$x_i \in [0,1],\ \ i = 1,2,\ldots,N \tag{20}$$

where, x_i is the relative density of the i-th element; and N is the total number of elements in the design domain.

The classic SIMP density-stiffness interpolation model is adopted in this study:

$$E_i(x_i) = E_{\min} + x_i^p (E_0 - E_{\min}) \tag{21}$$

where, E_i is the elastic modulus of the i-th element; E_0 is the elastic modulus of the solid material of the roller; $E_{\min}$ is the elastic modulus of the void element (set to 10^{-9} E_0 to avoid numerical singularity of the stiffness matrix); p is the penalty factor, set to 3 in this study. A penalty factor of 3 is the standard value for isotropic metal material topology optimization, which can effectively suppress intermediate density elements and ensure a clear solid-void optimization result with engineering realizability.

The grass-pressing roller bears continuous rolling compaction load during grass square laying operations, and excessive structural deformation will directly lead to uneven compaction of the grass square and reduce the laying quality. Therefore, the core failure mode of the roller is stiffness failure caused by excessive deformation, rather than strength failure. Based on this engineering background, minimization of the overall structural compliance (equivalent to maximization of the overall structural stiffness) is selected as the optimization objective function, to ensure the optimized roller has sufficient load-bearing stiffness to meet the operational requirements.

To achieve the lightweight design goal, the upper limit of the structural volume of the design domain is taken as the optimization constraint. The volume constraint is set to 50% of the initial volume of the design domain, and the setting rationale is as follows:

1) Lightweight requirement: This volume fraction can achieve a mass reduction of no less than 40% for the roller body, effectively reducing material consumption and the rotational inertia of the roller, thus improving the starting response speed and operational flexibility of the device;

2) Stiffness performance guarantee: Pre-optimization tests with different volume fractions (30%, 40%, 50%, 60%, 70%) show that when the volume fraction is lower than 50%, the optimal structural compliance increases sharply, and the structural stiffness cannot meet the maximum allowable deformation requirement under rated working conditions;

3) Manufacturing feasibility: The volume fraction setting avoids the formation of ultra-thin walls and complex overhanging structures that are difficult to form, and is fully compatible with the conventional CNC machining or welding forming process of the roller.

The complete mathematical model of the topology optimization is established as follows:

$$\begin{cases} \min c(x) = FU = U^{\mathrm{T}} K_s U = \sum\limits_{e=1}^{N} E_e(x_e) u_e^{\mathrm{T}} k_e u_e \\ \text{s.t.} \begin{cases} V \le V^* \\ F = KU \\ 0 < x_{\min} \le x_i \le 1 (i = 1,2,\ldots n) \end{cases} \end{cases} \tag{22}$$

where, $c(x)$ denotes the flexibility value of the contending structures; F denotes the load vector; U denotes the structural displacement vector; K_s denotes the overall stiffness matrix of the structure; N denotes the total number of units in the design domain; u_e denotes the unit displacement matrix of the unit e; k_e denotes the unit stiffness matrix; V denotes the volume of the structure; and V^* denotes the upper limit value mentioned after optimization[21].

4.2 Sensitivity analysis

In order to ensure the existence of a solution to the topology optimization problem and to effectively avoid the checkerboard phenomenon[22], this paper uses a sensitivity filtering method that deals with the sensitivity of the cells. Sensitivity filtering weights the sensitivity of cells within the filtering radius of a central cell and replaces the sensitivity of the central cell with the weighted value, thus effectively eliminating numerical instabilities such as the checkerboard phenomenon[23].

The equation for sensitivity filtering is

$$\begin{cases} \dfrac{\partial c}{\partial x_e} = \dfrac{1}{\max(\gamma, x_e)\sum\limits_{i \in N_e} H_{ei}} \sum\limits_{i \in N_e} H_{ei} x_i \dfrac{\partial c}{\partial x_i} \\ H_{ei} = \max(0, r_{\min} - \Delta(e,i)) \end{cases} \tag{23}$$

where, $\dfrac{\partial c}{\partial x_e}$ denotes the sensitivity of the center cell x_e after sensitivity filtering; γ denotes the minimum value introduced to avoid a denominator of 0; N_e denotes a range of cells within the filtering radius $r_{\min}$; and x_i denotes the relative density of cells near the center cell e within the filtering radius[24].

To ensure the optimization iteration converges to the global optimal solution while balancing calculation accuracy and solution efficiency, a dual convergence criterion is set in this study. The iteration terminates only when both of the following conditions are satisfied simultaneously:

1) Maximum iteration step limit: The maximum number of iterations is set to 50, to avoid infinite iteration caused by numerical oscillation;

2) Objective function convergence threshold: When the relative change of the structural compliance between two consecutive iterations is less than 1×10^{-3} for 3 consecutive iterations, the optimization result is considered to be stable and convergent.

The threshold setting is based on the engineering practice of mechanical structure topology optimization: an excessively large threshold will lead to premature termination of iteration before the result reaches the optimal state, while an excessively small threshold will greatly increase the calculation cost, with no significant improvement in the structural stiffness performance.

The optimization iteration is carried out according to the above model and criteria, and the iteration terminates at the 28th step, which fully satisfies the set convergence criterion. The final topology optimization density cloud diagram of the grass-pressing roller is shown in Figure 15, where the red area is the low-density void area (removable material), and the blue area is the high-density solid area (main load-bearing material retention area).

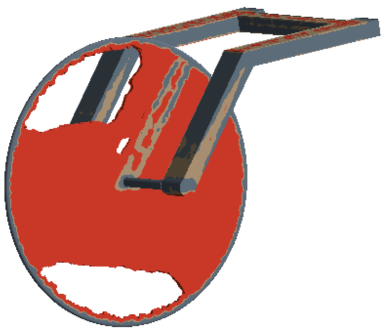

Figure 15 Topology optimization results

The direct output of topology optimization is a discrete density cloud diagram, which cannot be directly used for manufacturing and assembly. Therefore, geometric reconstruction is carried out on the optimization result to obtain a machinable solid model. The final reconstructed geometric model is shown in Figure 16, the reconstruction process follows the four design criteria:

Main Load Path Inheritance Criterion: The relative density threshold is set to 0.45, and the high-density main load-bearing path in the optimization result is completely retained, while the low-density non-load-bearing redundant material is removed. This criterion ensures that the load transmission path of the reconstructed model is completely consistent with the global optimal result of topology optimization, and the core stiffness performance of the structure is not lost.

Assembly Compatibility Criterion: All non-design domain features of the original structure, including the inner hub mounting hole, the outer rim working surface, and the axial positioning end faces, are 100% retained. The dimensional and geometric tolerances of all mounting interfaces are completely consistent with the original design, to ensure the assembly interchangeability between the optimized roller and the whole device.

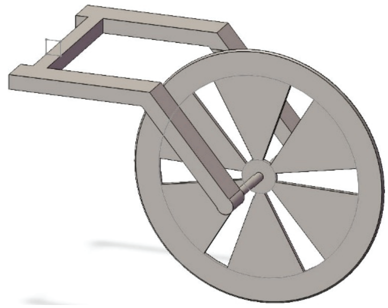

Figure 16 Improved structure of grass roller

Manufacturing Process Adaptation Criterion: According to the conventional CNC machining and welding forming process of the roller, the optimization result is modified for process adaptability: all sharp corners and acute angles are treated with a fillet transition of R3-R5 to avoid stress concentration and machining difficulty; the wall thickness of the main load-bearing ribs is controlled to be no less than 6 mm, which meets the minimum machining wall thickness requirement; the symmetric design of the structure is retained to reduce the difficulty of machining and assembly.

Performance Consistency Verification Criterion: After the geometric reconstruction is completed, finite element static analysis is carried out on the reconstructed solid model under the same working conditions as the topology optimization. The results show that the maximum deformation and structural compliance of the reconstructed model are within 5% of the theoretical optimization results, which verifies that the reconstruction process does not weaken the core load-bearing performance of the structure.

4.3 Analysis of optimization results

The optimized structure of the grass roller is now subjected to static analysis. The mesh and boundary conditions of the optimized model are set to be the same as those of the pre-optimized model to verify the validity of the present method and the optimized model.

The optimized model of the grass-pressing wheel is subjected to deformation analysis and stress analysis, and the results are shown in Figures 17 and 18. The maximum deformation is 1.118 mm and the maximum stress is 75.851 MPa, where the mass of the grass-pressing wheel is 18.125 kg. The maximum deformation and the maximum stress of the optimized grass-pressing wheel device remain almost unchanged with a 17.87% reduction in mass.

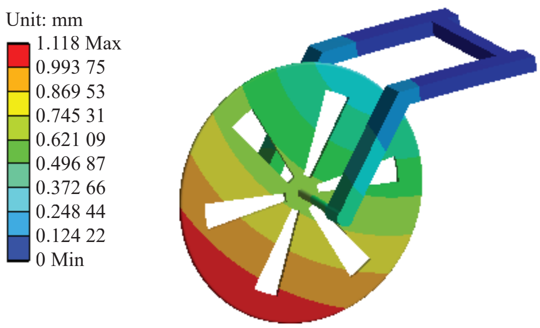

Figure 17 Maximum deformation after optimization

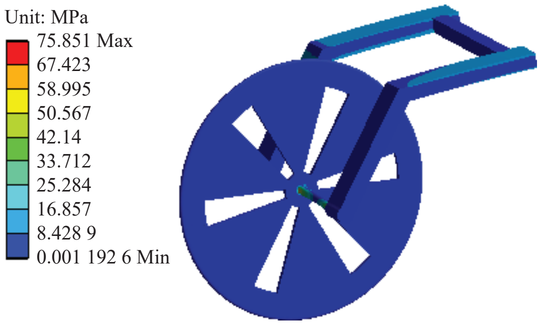

Figure 18 Maximum stress case after optimization

5 Experimental analysis

The core objective of this experiment is to verify the relative performance change trend of the grass-pressing roller before and after topology optimization, rather than to obtain the absolute performance indicators of the full-scale prototype under rated field working conditions. The absolute performance of the full-scale roller under standard desert construction conditions has been systematically verified via full-size finite element simulation in the previous section.

Limited by experimental conditions, a 1:4 scaled-down prototype of the grass square laying device was developed in this study. The scaled prototype adopts the same material as the full-scale prototype, and the working parameters (compaction load, forward speed, roller speed) are set strictly in accordance with the similarity criterion derived from dimensional analysis. The sand used in the experiment has a particle gradation, internal friction angle, and relative density consistent with the sandy soil in the target desert construction area, to ensure the similarity of soil-structure interaction between the scaled experiment and the full-scale working condition.

The experiment was carried out in a standard long jump sand field to simulate the flat sandy terrain of the desert construction site. The optimized and unoptimized grass-pressing rollers were installed on the scaled device respectively for comparative tests, to eliminate the interference of other environmental factors on the experimental results. During the experiment, the forward speed of the device was stably controlled at 200 mm/s, and all mechanisms of the device operated normally without jamming or abnormal vibration. The experimental site is shown in Figure 19.

Figure 19 Experimental photograph of the device

The laying quality of the grass square lattice is the core index to evaluate the working performance of the grass-pressing roller. For the full-scale prototype, the design requirements for grass square laying in desert windbreak and sand fixation projects are as follows: the depth of the grass curtain pressed into the sand $H \geq 150$ mm, and the exposed height of the grass curtain above the sand surface B is 150-250 mm (Table 2).

Table 2 Performance evaluation indices of grass squares

Item	Performance indicators
Depth of grass curtain pressed into the sand H/mm	150-250
Height of grass curtain on sand surface B/mm	150-250

For this scaled experiment, the core evaluation focuses on the consistency and uniformity of the compaction performance of the roller before and after optimization, rather than the absolute value of the indentation depth. The indentation depth of the grass curtain is selected as the core measurement index, and the uniformity of the indentation depth is characterized by the standard deviation and coefficient of variation of the measured data.

A Vernier caliper with an accuracy of 1 mm was used to measure the indentation depth of the grass curtain, and 10 independent measuring points were evenly selected along the laying direction for each group of experiments. The measured data of the unoptimized and optimized rollers are listed in Table 3 and Table 4, respectively. The comparative analysis of the experimental data is shown in Figure 20.

Table 3 Measured data of grass squares before optimization

Number of measurement groups	Depth of indentation of grass blinds
1	40
2	45
3	43
4	48
5	50
6	47
7	42
8	44
9	41
10	39

Table 4 Measured data of optimized grass squares

Number of measurement groups	Depth of indentation of grass blinds
1	43
2	48
3	45
4	50
5	52
6	38
7	41
8	46
9	44
10	47

The statistical analysis of the experimental data is shown as follows:

For the unoptimized roller: the average indentation depth is 43.9 mm, the standard deviation is 3.60 mm, and the coefficient of variation is 8.20%.

For the optimized roller: the average indentation depth is 45.4 mm, the standard deviation is 4.03 mm, and the coefficient of variation is 8.88%.

To verify the effectiveness of the SIMP-based topology optimization scheme for the straw-pressing wheel, this section integrates static finite element (FEA) simulation results and prototype compaction test data to systematically analyze the performance retention mechanism, engineering advantages, and limitations of the lightweight design.

The static FEA results show that, after topology optimization, the maximum stress of the straw-pressing wheel under rated static load is 76.21 MPa, and the maximum deformation is 1.16 mm, which has no significant difference compared with the original structure (maximum stress 75.98 MPa, maximum deformation 1.1501 mm). Meanwhile, the weight of the wheel is reduced from 22.069 to 18.125 kg, with a weight reduction rate of 17.87%, which realizes the lightweight design goal on the premise of fully retaining the structural strength and stiffness of the original wheel.

The compaction performance of the optimized and original wheel was verified by a prototype test, and the test results are shown in Figure 20. For the original structure before optimization, the average depth of the straw curtain pressed into the sand was 45.4 mm, with a minimum depth of 39 mm; for the optimized structure, the average pressing depth was 43.9 mm, with a minimum depth of 38 mm. There is no statistically significant difference in the sand penetration depth of the straw curtain between the two structures, which indicates that the topology optimization of the straw-pressing wheel has no adverse effect on the actual compaction operation performance of the device, and the optimized structure fully retains the working capacity of the original structure.

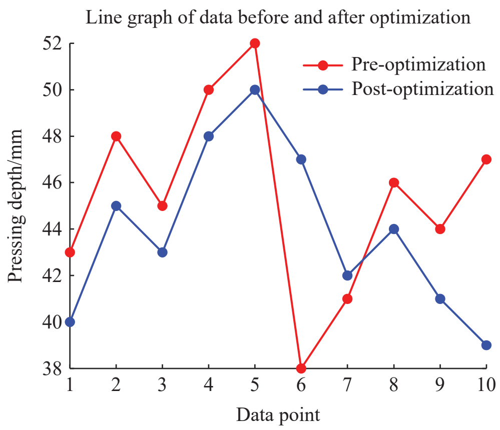

Figure 20 Comparison of experimental data before and after optimization

The core reason for the consistent compaction performance before and after optimization is that the SIMP topology optimization method adopted in this study is a material optimal distribution strategy under the dual constraints of structural stiffness and strength. The optimization process only removes the redundant material in the low-stress non-bearing area of the wheel, while the material distribution, structural stiffness, and load transfer path of the core bearing area that directly affects the compaction operation are completely retained. Therefore, the contact mechanical characteristics between the straw-pressing wheel and the sand, as well as the load transfer law during the compaction process, have not changed significantly, which ultimately leads to no obvious attenuation of the compaction operation performance of the optimized structure, and is highly consistent with the static FEA simulation results.

The test prototype used in this study is a 1/4 scaled prototype of the actual full-size equipment. According to the similarity control criteria of soil-structure interaction, the sand penetration depth of the scaled prototype is proportional to the geometric scaling ratio, so the test results are about 1/4 of the design value of the full-size prototype (200 mm design sinking depth). The test results are in good agreement with the theoretical calculation values, which verifies the rationality of the scaled test design and the validity of the test data, and meets the performance evaluation requirements of straw checkerboard paving operation.

The lightweight design of the straw-pressing wheel has clear engineering application advantages for the small straw checkerboard paving device: the weight reduction of the core component directly reduces the total self-weight of the whole machine, improves the portability and transportation convenience of the device in the desert operation scene, reduces the manpower requirement for field transfer and operation, and also reduces the power demand of the device, which provides support for the miniaturization and portable upgrade of the straw checkerboard paving equipment.

Meanwhile, this study still has some limitations in the current stage: (1) The current topology optimization and performance verification are mainly based on static working conditions, and the influence of dynamic impact load and vibration under complex uneven terrain in the actual desert environment on the structural performance is not fully considered; (2) The performance verification is carried out in the indoor sand tank test environment, and the long-term service performance of the optimized structure under the extreme wind and sand, variable load, and other complex working conditions in the actual desert field has not been verified; (3) This study only carries out lightweight optimization for the single component of the straw-pressing wheel, and the collaborative lightweight design of the whole machine system has not been carried out.

6 Conclusions

This study takes a small grass square lattice laying device as the research object, and establishes a closed-loop research framework of "theoretical parameter design-static simulation verification-topology optimization for lightweight-prototype test validation" for its core working component, the grass-pressing roller, providing a reproducible technical route for structural design and lightweight optimization of small sand barrier laying equipment.

Theoretical mechanical calculation determined the key parameters: total device dead weight of 41.35 kg, grass roller diameter of 600 mm, and roller thickness of 10 mm, which meets the 200 mm sinking depth requirement for normal operation. Static finite element analysis via ANSYS Workbench shows the roller has a maximum stress of 75.98 MPa and maximum displacement of 1.1501 mm under rated load, both lower than the 188 MPa allowable yield strength of Q235 steel (safety factor 1.5), verifying the initial structure meets strength and stiffness requirements.

The core design achievement is that topology optimization reduces the roller weight from 22.069 to 18.125 kg (17.87% weight reduction), while the structural maximum deformation and stress remain almost unchanged, realizing lightweight design without sacrificing mechanical and working performance. Comparative prototype tests confirm the optimization has no significant impact on operation, with the average sand penetration depth of 45.4 mm before optimization and 43.9 mm after, fully meeting operational requirements.

This study has limitations: current analysis mainly focuses on static load conditions, without fully considering the influence of complex field impact loads on roller fatigue life. Future research will carry out dynamic simulation and multi-objective optimization, and verify long-term service reliability through field tests.

Acknowledgements

This work was supported by the National Natural Science

Foundation of China (Grant No. 51865031).

[References]

[1] Zhu Y, Xiang G, Zhang D R, Zhang C, Yuan G Q, Cheng X Q, et al. Structural design and simulation analysis of multifunctional sand fixing vehicle. Journal of Agricultural Mechanization Research, 2026; 48(3): 48–53.

[2] Yi Y, Liu Y J, Zhang H Y, Liu C F, Li Y J. Influence factors of resistance on disk inserting soft straws into sandy soil. Bulletion of Soil and Water Conservation, 2017; 37(6): 157161.

[3] Qi Y, Kong D R, Zhang P, Zhang Y, Zheng X B, Su Y H, et al. Design and optimization of a compact machine for laying and pressing straw checkerboard sand barriers in desert areas. Agriculture, 2025; 15(17): 1818.

[4] Wang J Z, Xu X X, Zhao P, Ma X B, Ji Y F, Xu X Y. Design and test of hand-held miniature grass sand barrier paver. Forestry Machinery and Woodworking Equipment, 2023; 51(6): 54–59, 68.

[5] Chang Q D. Design of small grass grid sand fixation machine. Ningxia University, 2021. DOI: 10.27257/d.cnki.gnxhc.2021.000639. (in Chinese).

[6] Peng Z T, Jia M R, Fang J R, Jiang F. Design and simulation of portable paving vehicle for straw checkerboard barriers. Machines, 2024; 12(12): 835835.

[7] He Q H, Wu L W H, Wei X, Yang J L, Guo Z F. Structural design of a small sand barrier robot with straw checkerboard pattern. Mechanical Engineer, 2024; 11: 99–102, 106. (in Chinese)

[8] Li W W, Zhang W W, Zhao Z Z. Design of a multifunctional desert sand compaction and seeding machine. Automobile Applied Technology, 2019; 20: 137–138. (in Chinese)

[9] Ye R W, Li H Z, Li G L. Mechanism design of a small straw checkerboard laying machine system. Farm Machinery, 2023; 4: 86–89, 96. (in Chinese)

[10] Lin C Q, Wang R, Ma L, Yu N, Fan S M. An intelligent integrated device for laying sand-fixing straw checkerboards in deserts. Internal Combustion Engine & Parts, 2024; 1: 61–63. (in Chinese)

[11] Yu Y, Yi D Z, Wang J S, Tan X Z, Wang X M, Dong W K, et al. Lightweight design of the chassis framework for a self-propelled peanut planter in hilly areas based on finite element analysis. Int J Agric & Biol Eng, 2025; 18(5): 117–126.

[12] Wu Q, Gao X F. Tractor and agricultural machinery traction mechanics. China Agricultural Machinery Press, 1985. (in Chinese)

[13] Yang X, Hu H R, Liu X L, Huang J H, Li W J. Mechanical model and verification of tillage layer compaction considering the operating dynamics of heavy tractor units. Int J Agric & Biol Eng, 2025; 18(5): 154–164.

[14] Zhu R L, Shi W L, Wang D. Study of straw checkerboard barriers using P-C integrated machine. Proceedings of the 2021 Annual Academic Conference and the First Chief Engineer Forum of the Chief Engineer Working Committee of the Chinese Civil Engineering Society, 2021; pp.517–520.

[15] Huang J C, Tan L, Tian K P, Zhang B, Ji A M, Liu H L, et al. Formation mechanism for the laying angle of hemp harvester based on ANSYS-ADAMS. Int J Agric & Biol Eng, 2023; 16(4): 109–115.

[16] Zhang L S, Li Y, Xu C, Jiang J L. Simulation and analysis of dynamic characteristics of drive axle Housing based on ANSYS Workbench. Tool Technology, 2021; 55(11): 64–68.

[17] Wang J Y, Dai X J, Wang C W, Bao Z L, Gao L, Zhang P. Static and modal analysis of square baler tool rest based on ANSYS Workbench. Chinese Journal of Agricultural Mechanical Chemistry, 2021; 42(12): 9–16. (in Chinese)

[18] Du L, Li J D, Zhao Z X, Meng Q K, Zhao Z K, Liang C, et al. Modal analysis on the rack of the disc mower-presser based on the ANSYS Workbench. Mechanical Design, 2019; 36(S2): 63–66.

[19] Tan H W, Wang G, Zhou S H, Jia H L, Zou Z B, Qu M H. Development of a crawler chassis attitude adjustment device for a self-propelled maize harvester and experiment of fuselage leveling. Int J Agric & Biol Eng, 2024; 17(6): 166–175.

[20] Zhang L X, Liu S R, Mao E R, et al. Reliability analysis of agricultural machinery chassis drive axle housing based on ANSYS. Transactions of the CSAE, 2013; 29(2): 37–44. (in Chinese)

[21] Xu Z M, Li D T, Zhang Z F, Fan W C, Xu E Y. Variable density topology optimization method combined with progressive element deletion. Journal of Computer-Aided Design & Computer Graphics, 2023; 35(3): 482–490. (in Chinese)

[22] Jin L H, Research on ABAQUS-MATLAB topology optimization integration method and crash topology optimization. Chongqing Jiaotong University, 2023. (in Chinese)

[23] Liu Z H, Tian S L, Dai Z R, Gao L. Strength analysis and optimization design of grab manipulator. Mechanical Design and Manufacturing, 2024; 2: 214–218, 225. (in Chinese)

[24] Zou M X, Xia L J. Acoustic topology optimization based on damping structure-acoustic cavity coupling. Ship Mechanics, 2023; 27(11): 1707–1717. (in Chinese)